JOURNAL OF GEOPHYSICAL RESEARCH, VOL. 114, D09108, doi:10.1029/2008JD011159, 2009

On the late northward propagation of the West African monsoon in summer 2006 in the region of Niger/Mali

P. Drobinski,[1] S. Bastin,[2] S. Janicot,[3] O. Bock,[2,4] A. Dabas,[5] P. Delville,[6] O. Reitebuch,[7] and B. Sultan[3]

Received 18 September 2008; accepted 4 March 2009; published 13 May 2009.

[1] This paper investigates the fine-scale dynamical processes at the origin of the late northward migration of the monsoon flow in summer 2006 in the region of Niger and Mali (onset on 3 July 2006 compared to the climatological onset date, 24 June). Compared to a 28-year climatology, 2006 NCEP-2 reanalyses show evidence of an anomalous pattern during 10 days between 25 June and 3 July 2006, characterized by the African Easterly Jet (AEJ) blowing from the northeast along a narrow northeast/southwest band located over the Hoggar and Air mountains associated with an unusually strong northeasterly harmattan in the lee of the mountains. Using data collected during the African Monsoon Multidisciplinary Analysis (AMMA) experiment and mesoscale numerical simulations, this study shows evidence of interaction between the AEJ and the orography supported by the reduced gravity shallow water theory which explains the enhancement of the harmattan downstream of the Hoggar and Air mountains in summer 2006. The enhanced harmattan contributes to move southward the intertropical discontinuity (ITD) defined as the interface between the cool moist southwesterly monsoon flow and the warm dry harmattan. Finally, an interaction between the ITD and African Easterly waves contributes to propagate the ITD southward retreat about 1500 km to the west of the Hoggar and Air mountains.

Citation: Drobinski, P., S. Bastin, S. Janicot, O. Bock, A. Dabas, P. Delville, O. Reitebuch, and B. Sultan (2009), On the late northward propagation of the West African monsoon in summer 2006 in the region of Niger/Mali, *J. Geophys. Res.*, *114*, D09108, doi:10.1029/2008JD011159.

1. Introduction

[2] Rainfall over West Africa is linked to the meridional migration of the Intertropical Convergence Zone (ITCZ). Following the migration of the Sun the monsoon develops during the northern spring and summer, bringing the ITCZ and the associated rainfall maxima to their northern location in August [*Hastenrath*, 1995]. As the West African societies are highly vulnerable to the monsoon rainfall variability, understanding the basic processes of the West African monsoon (WAM) northward propagation and especially of its onset is a key scientific and societal issue.

[3] West African monsoon has been widely studied using synoptic-scale reanalyses [*Janicot et al.*, 2001; *Sultan and Janicot*, 2003; *Drobinski et al.*, 2005; *Sultan et al.*, 2007], satellite imagery [*Yang and Slingo*, 2001; *Mohr*, 2004] or dropsonde measurements along south-north aircraft transects [*Parker et al.*, 2005]. Many processes, in particular the interactions between synoptic-scale and mesoscale dynamics, are still not well observed, described and understood, leading to recurrent problems in simulating the WAM rainfall in weather or climate models [e.g., *Lebel et al.*, 2000; *Yang and Slingo*, 2001].

[4] A key issue is to better understand the processes which contribute to the monsoon onset since its date determines the optimal seeding period (in the Sahel, rainfed crop production is the main source of food and income of one of the world's most rapidly growing populations). *Sultan and Janicot* [2003] showed that the onset of the monsoon is linked to an abrupt shift of the ITCZ from a quasi-stationary location at 5°N in May-June to another stationary location at 10°N in July-August, and the associated intertropical discontinuity (ITD, defined as the interface between the cool moist southwesterly monsoon flow and the warm and dry northeasterly harmattan flow) from 17°N in May-June to 20°N in July-August [*Sultan and Janicot*, 2003; *Sultan et al.*, 2007]. *Sultan and Janicot*

---

[1] Laboratoire de Météorologie Dynamique, Institut Pierre Simon Laplace, École Polytechnique, ENS, UPMC, CNRS, Palaiseau, France.

[2] Service d'Aéronomie, Institut Pierre Simon Laplace, UPMC, UVSQ, CNRS, Paris, France.

[3] Laboratoire d'Océanographie et du Climat: Expérimentation et Approches Numériques, Institut Pierre Simon Laplace, UPMC, IRD, MNHN, CNRS, Paris, France.

[4] Laboratoire de Recherche en Géodésie, Institut Géographique National, Marne la Vallée, France.

[5] Centre National de Recherches Météorologiques, Météo-France, Toulouse, France.

[6] Division Technique, Institut National des Sciences de l'Univers, CNRS, Meudon, France.

[7] Institut für Physik der Atmosphäre, Deutsches Zentrum für Luft- und Raumfahrt, Oberpfaffenhofen, Germany.

0148-0227/09/2008JD011159

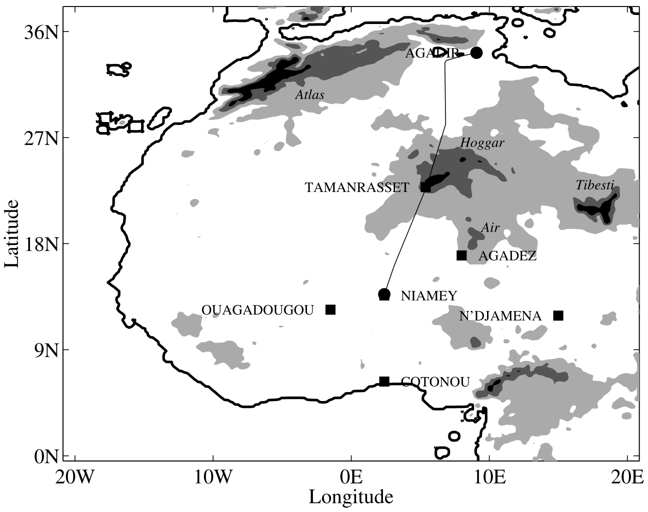

Figure 1. Geographic map of North and West Africa with geographical labels (main orographic features appearing in italic). The increment for the contour lines is 500 m, from 500 m to 1500 m altitude. The leg flown by the DLR Falcon 20 between 0850 and 1235 UTC on 30 June 2006 is shown with a solid line. The black dots indicate the starting and ending points of the DLR Falcon 20 track, and the black squares indicate the radiosounding station locations.

[2003] showed that the distribution of the monsoon onset dates (hereafter referred as t_0) is characterized by a mean on 24 June and a standard deviation of 8 days. The monsoon onset corresponds to a transition period of weaker convection during several days and is accompanied with major changes in the atmospheric dynamics.

[5] Presently few studies have investigated the possible mechanisms controlling the monsoon onset [*Sultan and Janicot*, 2003; *Drobinski et al.*, 2005; *Ramel et al.*, 2006; *Sijikumar et al.*, 2006; *Hagos and Cook*, 2007]. *Sultan and Janicot* [2003] observed at the time of the monsoon onset the enhancement of the Saharan heat low (SHL) in terms of horizontal and vertical circulation. They suggested that this favors both convective inhibition through intrusion of dry and subsiding northerly air and an enhancement of conditional instability through a greater inland moisture advection and a higher monsoon depth. Afterward the accumulated instability breaks the convective inhibition. At the time of the monsoon onset the deepening of the SHL has also been observed due to an interaction with the northern Africa orography [*Sultan and Janicot*, 2003; *Drobinski et al.*, 2005]. As the ITCZ moves to the north and deep convection intensifies, the northern Hadley-type circulation fully develops, contributing to enhance the subsiding branch of the northern Hadley-type cell over and northward of the Atlas-Hoggar mountains (see Figure 1) and the associated northeasterly winds. This leads to an increase and a southeasterly-northeasterly rotation of the low-level wind ahead of the Hoggar which contribute to an increased leeward-trough effect enhancing the Saharan heat low [*Drobinski et al.*, 2005]. *Ramel et al.* [2006] showed also by performing a regional model simulation that this low-level wind rotation induces a warmer air mass advection over the western Sahara decreasing the sensible heat flux in this area, then allowing a rapid increase in the surface temperature and an additional deepening of the heat low. *Hagos and Cook* [2007] confirmed the previous investigations through the analysis of the moisture, momentum and energy budgets around the monsoon onset in a regional simulation. They highlighted also the role of inertial instability to explain the abrupt shift of the ITCZ at this time of the annual cycle of the African monsoon.

[6] Following the definition of the onset date proposed by *Sultan and Janicot* [2003], the monsoon onset occurred very late in 2006 during the African Monsoon Multidisciplinary Analysis (AMMA) program, around 3 July (t_0 in 2006) [*Janicot et al.*, 2008], that is 10 days after the mean onset date, which corresponds to a cumulative probability of occurrence of 10% (i.e., 10% of the onsets occurred on and after 3 July). In this article, we show that the week preceding the onset date t_0 in 2006 displays anomalous atmospheric features in comparison with the climatology. During this anomalous preonset period, on 30 June 2006 (i.e., $t_0 - 3$ days), the French-German airborne Doppler lidar WIND (Wind Infrared Doppler lidar) flew along a north-south transect from Djerba (Tunisia) to Niamey (Niger) above the Hoggar and Air mountains (see Figure 1), providing the wind field in a two-dimensional plane along the flight track which contributed to document the African Easterly Jet (AEJ) blowing over the mountains and the location of the ITD separating the southwesterly monsoon flow from the northeasterly harmattan. This data set associated with mesoscale simulations using the NCAR-Advanced Research WRF numerical model, provide arguments to explain the origin of the preonset anomaly and the late onset of the monsoon flow which persistency and horizontal extent are analyzed using NCEP-2 reanalyses. The $t_0 - 3$ days date is thus used in this study as a referenced date since it appeared to be a representative day of this unusually late preonset period.

[7] We show that the abnormal westward shift of the Libyan anticyclone leads to a strong interaction between the AEJ and the Hoggar and Air massifs which causes the reinforcement of the harmattan downstream. This prevents the northward propagation of the ITD and may have contributed to the delayed monsoon onset. This mechanism is highlighted for the first time as complementary to the leeward-trough effect enhancing the Saharan heat low.

[8] Section 2 details the summer 2006 anomaly using the NCEP-2 reanalyses, its pattern, duration and propagation. Section 3 analyzes the fine-scale processes contributing to this anomaly, especially the AEJ/mountain interactions, explaining in part the late northward propagation of the WAM in summer 2006. Section 4 concludes the study and suggests future work.

2. Summer 2006 Anomaly in NCEP-2 Reanalyses

2.1. NCEP-NCAR Reanalyses

[9] The National Center for Environmental Prediction (NCEP) and the National Center for Atmospheric Research (NCAR) have completed a reanalysis project with a current version of the Medium Range Forecast (MRF) model [*Kalnay et al.*, 1996]. This data set consists in a reanalysis of the global observational network of meteorological variables (wind, temperature, geopotential height, humidity

Table 1. West African Radiosoundings Assimilated in 2006 in NCEP-2 Reanalyses[a]

ID	Jan	Feb	Mar	Apr	May	Jun	Jul	Aug	Sep	Oct	Nov	Dec	Station
08594	22	28	30	29	31	29	28	33	44	27	30	24	Sal
60680	62	56	63	60	62	118	121	123	90	62	57	60	Tamanrasset
61024	49	43	52	59	62	159	125	125	118	58	29	30	Agadez
61052	61	44	66	83	121	159	122	136	119	115	116	123	Niamey
61223	0	0	0	0	0	0	2	1	1	3	0	2	Tombouctou
61291	27	30	53	57	53	54	54	52	56	57	54	60	Bamako
61415	3	4	0	1	0	1	0	3	11	27	16	10	Nouadhibou
61442	12	13	28	27	24	18	3	12	13	24	19	27	Nouakchott
61641	27	33	62	58	62	60	60	59	56	61	55	61	Dakar
61687	2	14	30	19	0	17	23	33	28	29	0	0	Tambacounda
63450	4	7	7	2	3	10	25	24	22	27	22	23	Addis Abeba
64650	0	0	0	0	8	11	13	1	0	0	0	11	Bangui
64700	13	14	28	53	61	59	57	34	49	57	16	0	N’Djamena
64870	5	3	5	12	8	16	22	20	8	17	14	7	Ngaoundere
64910	22	33	60	41	42	47	51	50	53	56	53	53	Douala
65125	0	0	0	0	0	0	5	129	12	16	24	30	Abuja
65330	0	0	0	0	0	0	21	110	54	11	19	25	Parakou
65344	5	0	6	22	25	133	109	81	110	56	50	57	Cotonou
65418	0	0	0	0	1	2	2	72	68	3	1	0	Tamale
65503	12	6	24	0	30	53	57	44	26	11	0	31	Ouagadougou
65578	0	0	0	0	0	0	7	13	11	29	17	0	Abidjan

[a] Courtesy of B. Ballish. ID is the WMO station code. For legibility, only the locations of the radiosoundings launched from Agadez (Niger), Cotonou (Benin), N’Djaména (Chad), Niamey (Niger), Ouagadougou (Burkina Faso), and Tamanrasset (Algeria), i.e., in the vicinity of the DLR Falcon 20 flight track, are shown in Figure 1 and analyzed in section 3.

on pressure levels, surface variables, and flux variables like precipitation rate) with a “frozen” state-of-the-art analysis and forecast system at a triangular spectral truncation of T62 to perform data assimilation from 1948 to present. This circumvents problems of previous numerical weather prediction analyses due to changes in techniques, models and data assimilation. Data are reported on a 2.5° × 2.5° grid every 6 hours (0000, 0600, 1200 and 1800 UTC), on 17 pressure levels from 1000 to 10 hPa, which is sufficient for capturing synoptic-scale variability. This study uses the NCEP/DOE AMIP-II Reanalysis (Reanalysis-2, hereafter referred as NCEP-2) based on the NCEP-NCAR reanalysis but with improvements of the physical parameterizations and error fixes [*Kanamitsu et al.*, 2002]. We use here the data covering the 1979–2006 period with four values per day.

[10] Before the AMMA intensive field experiment of summer 2006, the West African soundings assimilated in NCEP-2 reanalyses were few since only a small set of sounding stations were operated regularly. Dakar, Bamako, Ouagadougou Agadez and Niamey were the only stations south of Sahara providing 1 (or 2 for Dakar and Niamey) soundings per day. In 2006 the sounding network has been highly enhanced and is still working very well nowadays (see Table 1).

2.2. Anomalous Pattern of the Atmospheric Circulation at the African Continent Scale

[11] Figure 2 shows the 1200 UTC synoptic charts from the NCEP-2 reanalysis at $t_0 - 3$ days during the preonset period of summer 2006, i.e., on 30 June 2006. The 500-hPa field (Figure 2a) shows an anticyclonic region over North Africa which corresponds to the descending branch of the Hadley cell. This anticyclone is generally referred as the anticyclone of Libya. During the preceding days, the anticyclone moved westward contributing to give a slanted southwest/northeast orientation to the AEJ over central Africa which is visible on the analyses at 500 hPa. The AEJ is associated with very dry air, the relative humidity never exceeding 25% and often below 5% (such dry-air structures, probably conveyed by the AEJ, originate in the upper levels (200–250 hPa) on the anticyclonic side of the polar jet stream at 50°N [see *Roca et al.*, 2005]). A similar AEJ structure is also found at 700 hPa which is often the chosen level to diagnose the AEJ by the forecasters. At the surface, a region of low mean sea-level pressure is located between 15°N and 20°N (Figure 2c), and is referred as the Saharan heat low, the dynamics of which has been studied in the past few years [*Rácz and Smith*, 1999; *Parker et al.*, 2005; *Drobinski et al.*, 2005; *Ramel et al.*, 2006; *Peyrillé and Lafore*, 2007; *Peyrillé et al.*, 2007]. The heat low meridional circulation intensity is the highest at the beginning of the monsoon onset, leading to both an increase in convective inhibition in the ITCZ through intrusion of dry and subsiding air from the north increasing the capping inversion, and an increase in conditional instability through a greater inland moisture advection. The inland penetration of moisture with the monsoon flow is visible in Figure 2d which shows the surface wind and relative humidity. The southwesterly monsoon flow penetrates inland as far as 17°N, referred as the intertropical discontinuity (ITD) (where the relative humidity drops below 30% and where the wind direction shifts from the southwest to the northeast, see the thick dashed line in Figure 2d). The smooth gradient of humidity between the coast where it reaches 80–90% and the ITD is partly associated with the gradient of land use (land cover, vegetation) and properties (soil type, soil moisture and temperature, etc.) [*Zheng and Eltahir*, 1998] and partly with the climatological circulation.

[12] In Figures 3 and 4, the 2006 charts at $t_0 - 3$ days (i.e., 30 June 2006) are compared to the composite 28-year mean fields computed from the 4 times daily NCEP-2 reanalyses at $t_0 - 3$ days between 1979 and 2006. Figure 3 shows the mean charts, similar to those displayed

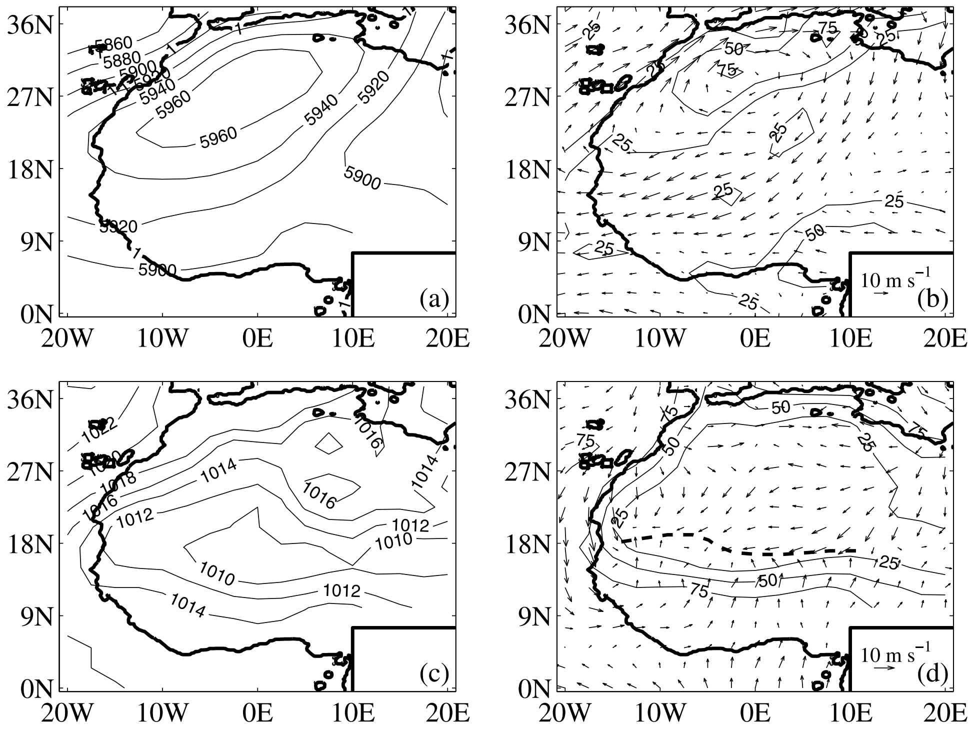

Figure 2. NCEP-2 reanalysis on 30 June 2006 ($t_0 - 3$ days) at 1200 UTC: (a) 500-hPa geopotential, (b) 500-hPa wind and relative humidity, (c) mean sea level pressure, and (d) surface wind and relative humidity. The thick dashed line in Figure 2d displays the location of the intertropical discontinuity (ITD) where the wind direction shifts from the southwest to the northeast.

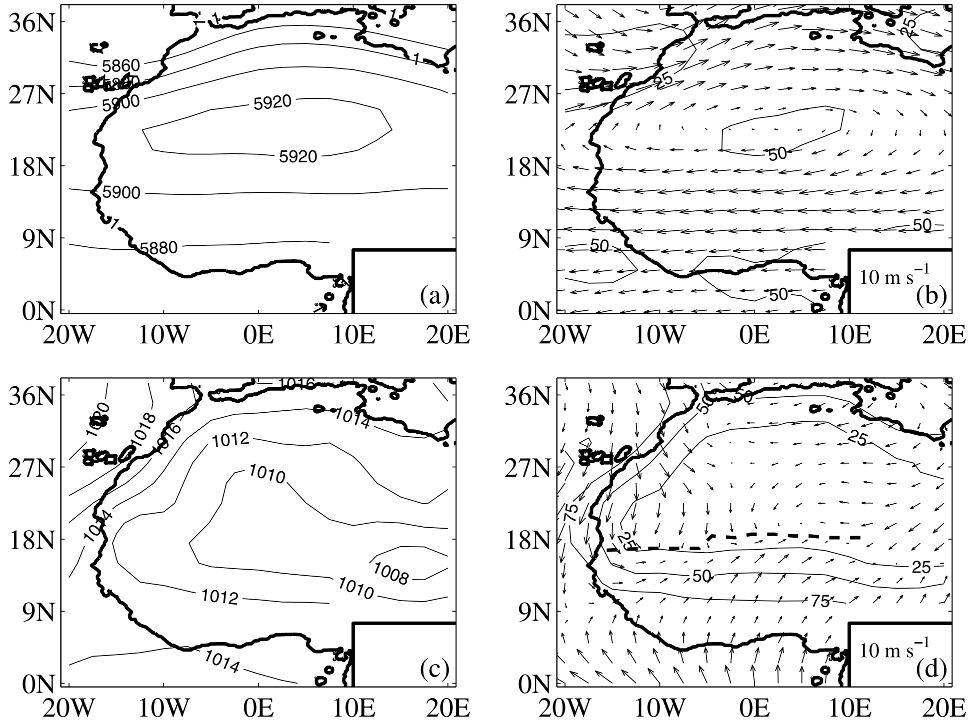

Figure 3. Same as Figure 2 for the 28-year composite obtained from the NCEP-2 reanalyses at $t_0 -$ 3 days.

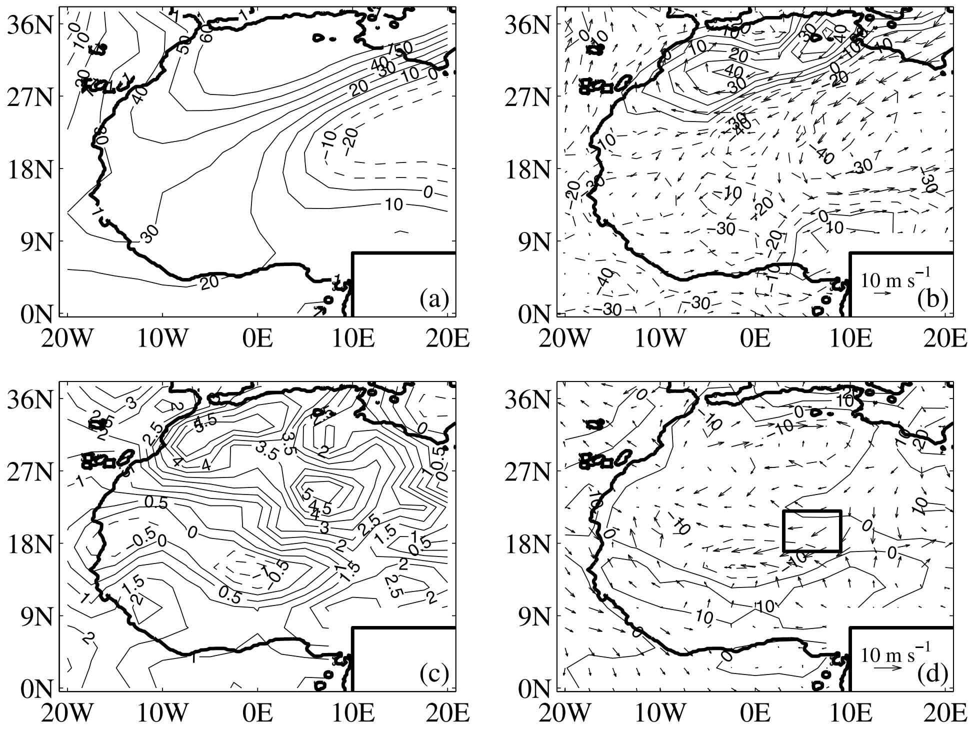

Figure 4. Difference between the 2006 synoptic charts (Figure 2) and the NCEP-2 climatology (Figure 3) at $t_0 - 3$ days. The box in Figure 4d displays the region in the lee of the Hoggar and Air mountains where the harmattan is unusually strong in late June 2006. The solid and dashed isocontours indicate positive and negative anomalies, respectively.

in Figure 2. The 500-hPa pattern reveals an eastward extension of the anticyclone of Libya and a more zonal orientation than during the 2006 preonset period (Figure 3a). The high-pressure system is also weaker in the climatology. The climatological AEJ has a pronounced zonal orientation and the core of the jet is located at about 14°N.

[13] Figure 4 shows that the midtropospheric air is also much drier in 2006 with differences ranging between 20% and 60%.

[14] In 2006, the ITD reaches at most 17°N at $t_0 - 3$ days whereas its climatological location is around 20° between 8°W and 10°E (see thick dashed line in Figures 2d and 3d). Figure 4d shows evidence of a reinforcement of the near-surface flow descending the slopes of the Hoggar and Air mountains in 2006 (see box in Figure 4d). The question is thus whether there exists a relation between the anomalous location of the AEJ and the reinforcement of the harmattan and consequently whether a persistent unusual location of the AEJ over the Hoggar and Air massifs can force an unusually persistent and strong harmattan flow on the descending slope of the mountain to the ITD.

2.3. Anomaly Duration and Propagation

[15] Figure 5 displays the summer 2006 wind speed "anomaly" at the surface and 500 hPa with respect to the climatology, at 1200 UTC. One must note that the trend is similar at night but the location of the ITD differs with respect to its daytime location [*Sultan et al.*, 2007]. In order to minimize the variability of the ITD location which worsens the legibility of the images, we only show the comparison at 1200 UTC.

[16] Figure 5 reveals a strong reinforcement of the 500-hPa wind speed starting at $t_0 - 8$ days with a strengthening of the northerly component followed by the easterly component, and ending at about t_0. The wind reinforcement extends between the surface and about 500 hPa and is maximum between 2°E and 8°E and between 19°N and 24°N even though it extends farther west but with a weaker signal. This period corresponds to the displacement of the AEJ from its climatological location to its northeast/southwest orientation over the Hoggar and Air massifs, and justifies the choice of 30 June 2006 ($t_0 - 3$ days) as a representative day of the late preonset period. At the same period, the easterly component of the 10-m wind speed increases and a comparatively weak reinforcement of the northerly component (weaker than 1 m s^{-1}) is also visible, which is consistent with the presence of the AEJ over the mountains during this period. The diurnal variation of the anomaly does not show evidence of any diurnal modulation of the harmattan intensity, since the average value of the anomaly (about 4 m s^{-1}) is similar during daytime and nighttime, but the standard deviation of the anomaly is much larger from day to day during daytime (1.7 m s^{-1}) than during nighttime (0.9 m s^{-1}). The presence of this enhanced downslope wind during more than a week after the climatological WAM onset date [*Sultan and Janicot*, 2003] may partly explain the late northward propagation of the WAM downstream of the Hoggar and Air massifs.

[17] Figure 6 displays the latitudinal location of the ITD in 2006 and from the climatology, as a function of time between 2°E and 8°E, between 2°E and 4°W, between 4°W and 10°W, and between 10°W and 16°W. The location of

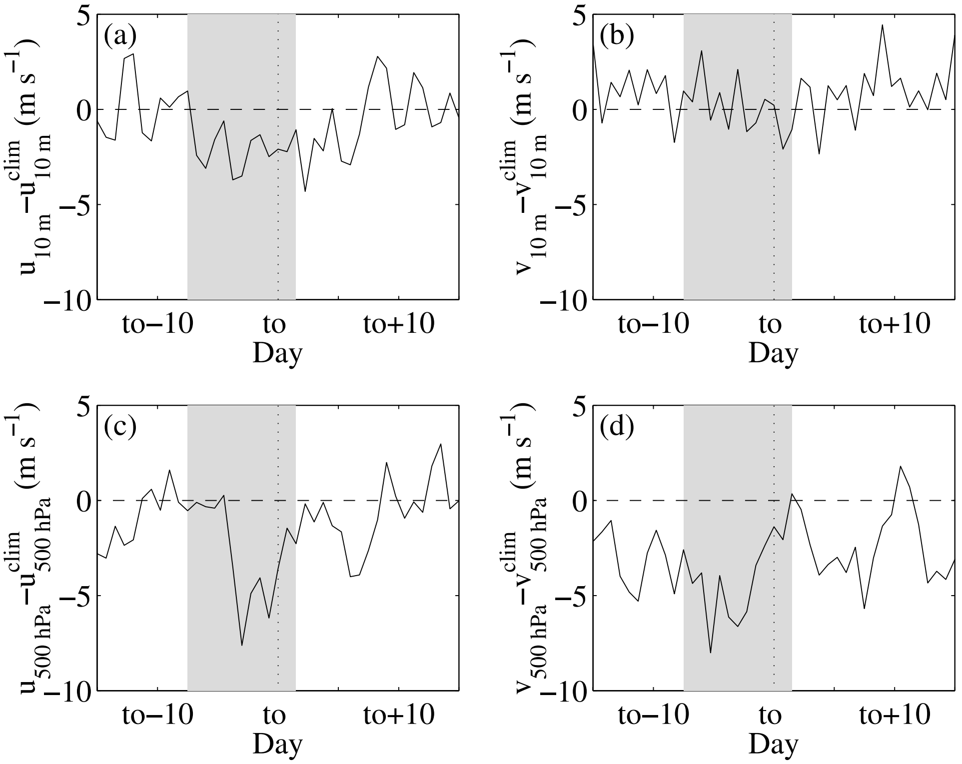

Figure 5. Difference between the (left) NCEP-2 zonal and (right) meridional wind components at 1200 UTC in June-July 2006 and (a and b) from the NCEP-2 climatology at 10-m above ground and (c and d) at 500 hPa, averaged over the region (2°E−8°E; 19°N−24°N).

the ITD is defined as latitudinal location of the shift between the southerly monsoon flow and northerly harmattan diagnosed from the NCEP-2 surface wind field for summer 2006, and from the mean NCEP-2 surface wind field for the climatology. Figure 6 shows a smooth increase as a function of time of the climatological location of the ITD between 2°E and 8°E (about 8 km per day). The increase of the ITD location as a function of time is stronger west of the lee of the Hoggar and Air massifs (about 19, 14 and 10 km per day between 2°E and 4°W, between 4°W and 10°W, and between 10°W and 16°W, respectively).

[18] We can see that between 2°E and 8°E, i.e., downstream of the Hoggar and Air massifs (see box in Figure 4d), the ITD location in 2006 agrees well with the climatological location (less than 0.5°) except between $t_0 - 8$ days and t_0 when the difference can reach 2°. The period when the ITD moves back corresponds to the reinforcement of the upper level and surface flow downstream of the Hoggar and Air massif (Figure 5). We can also see in Figures 6b and 6c a westward propagation of the ITD southward retreat starting $t_0 - 5$ days between 4°W and 10°W, which gives a westward propagation of about 4° per day, i.e., about 5 m s^{-1}. The ITD retreat is not visible between 10°W and 16°W because the detection of the ITD location becomes noisier west of 2°E–8°E since the monsoon flow/harmattan transition is much smoother.

[19] The propagation speed of 5 m s^{-1} is consistent with the phase speed for African Easterly waves (AEW) [e.g., *Reed et al.*, 1977; *Diedhiou et al.*, 1999; *Hsieh and Cook*, 2005]. We thus evaluate AEW activity in the latitude band ranging from 5°N to 20°N to check for a possible correlation between the westward propagation of the ITD southward retreat and the passage of an AEW in the lee of the Hoggar and Air mountains $t_0 - 8$ days. Previous studies [e.g., *Reed et al.*, 1977] have used AEJ level trough and ridge axes, generally defined by a change in sign of the meridional wind field (i.e., $v = 0$ m s^{-1}), as the definition for an AEW. Figure 7 shows the Hovmöller space-time diagram of the 2- to 6-day band-pass-filtered meridional wind at 700 hPa averaged between 5°N and 20°N.

[20] We can see an AEW detected at 700 hPa passing over the longitude band (2°E;8°E) $t_0 - 8$ days and reaching the longitude band (4°W;10°W) 2 days later, in agreement with *Thorncroft et al.* [2007] classification. The AEW is thus a possible candidate for the westward propagation of the ITD southward retreat end of June beginning of July 2006, by a modulation of the surface pressure. However, the question whether the ITD retreat and the AEW dynamics are part or not of one single mechanism (the mountains contributing both to the ITD retreat and the AEW initiation [see *Zehnder et al.*, 1999]) requires a more rigorous identification of the relationship between the ITD and the AEW, and a dedicated study which is out of the scope of this paper and is left for future work.

3. Fine-Scale Processes

[21] In this section, the fine-scale dynamical processes contributing to the harmattan enhancement and the ITD retreat are investigated by using the AMMA observations and mesoscale simulations as downscaling tool for a more accurate identification of the ITD location and its modula-

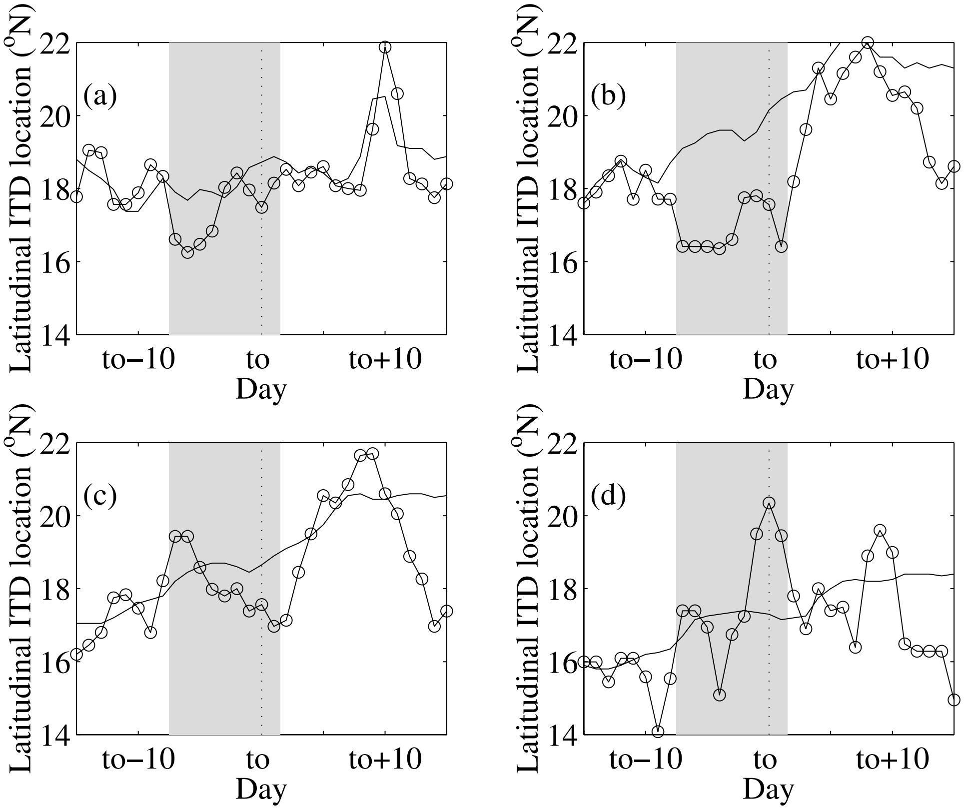

Figure 6. Location of the ITD as a function of time defined as latitudinal location of the shift between the southerly monsoon flow and northerly harmattan diagnosed from the NCEP-2 surface wind field. The solid line corresponds to the climatological ITD, and the circles correspond to the 2006 ITD. The ITD location is obtained from the 10-m wind averaged (a) between 2°E and 8°E, (b) between 2°E and 4°W, (c) between 4°W and 10°W, and (d) between 10°W and 16°W.

tion in time and longitude due to the higher model resolution; and for deriving hydraulic diagnostics for a better understanding of the harmattan acceleration downstream of the Hoggar and Air massifs.

3.1. Summer 2006 Monsoon

3.1.1. Observation and Mesoscale Simulation of the Monsoon Onset

[22] The GPS (Global Positioning System) data allow to estimate the integrated water vapor (IWV) in the atmospheric column and document its variability from subdiurnal to intraseasonal time scales [*Bastin et al.*, 2005a, 2006a; *Bock et al.*, 2007]. In the framework of AMMA, six GPS stations were installed in a domain covering 2°W–2°E and 9°N–17°N along two different meridian transects, each composed of three GPS stations located in three zonal bands of variable land cover, to complement observations from existing GPS network (Dakar, Yamassoukro and Libreville). One transect, centered on 0°–2°E (Djougou, Niamey and Gao) measured continuously IWV between 2005 and 2007, while the second transect, (Tamale-Ouagadougou-Tombouctou) was deployed only during 2006. Figure 8 shows the evolution of the IWV over the full monsoon season of 2006 at three sites (Niamey (2.4°E;13.5°N), Gao (3°W;16.3°N), and Tombouctou (3°W,16.7°N)), as observed with GPS. The IWV content remains around 40 kg m^{-2} at Niamey and 30 kg m^{-2} at Gao and Tombouctou until t_0, when the IWV increases almost linearly up to above 35 kg m^{-2} until the monsoon retreats. The ITD is located close to the latitude of Gao, where oscillations with about 10 days periodicity are measured and which correspond to alternations of large-scale advections of moist air from the south and dry air from the north accompanying the passage of the ITD at that site.

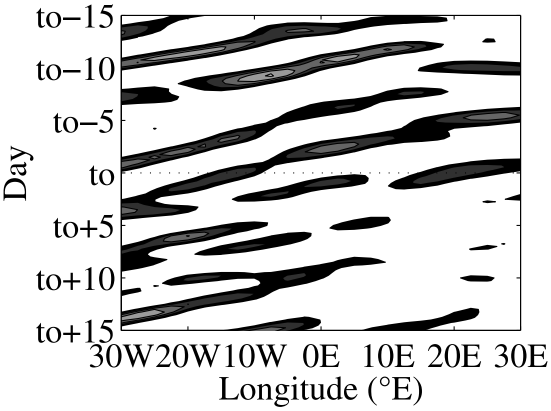

Figure 7. Hovmöller space-time diagram of the 2- to 6-day band-pass-filtered NCEP-2 meridional wind at 700 hPa averaged between 5°N and 20°N (shaded every 1 m s^{-1} above +1 m s^{-1}).

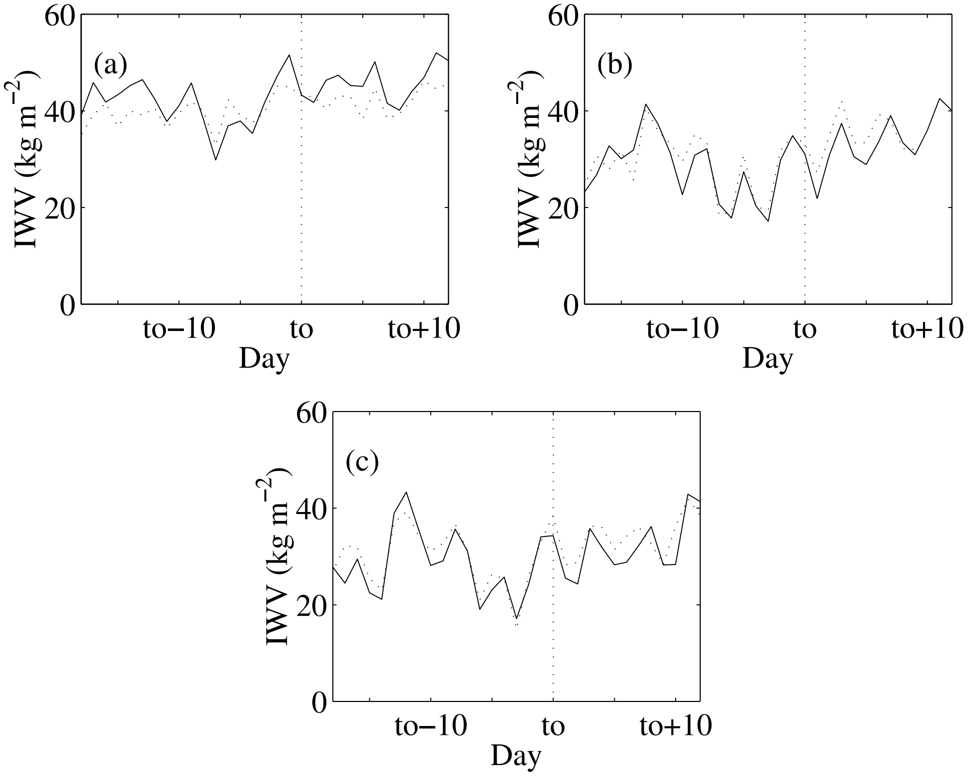

Figure 8. IWV as measured by three GPS receivers (dotted lines) located in (a) Niamey (2.4°E;13.5°N), (b) Gao (3°W;16.3°N), and (c) Tombouctou (3°W,16.7°N) and simulated by WRF (solid lines) from $t_0 - 18$ to $t_0 + 12$.

[23] At shorter time scales, a phase of strong fluctuations in IWV is observed, especially at Gao and Tombouctou. The periodicity then is about 3–5 days, consistently with AEW discussed in section 2.3.

[24] The monsoon variability, the location of the ITD, its modulation in time and longitude, were also investigated using the nonhydrostatic Weather Research and Forecasting (WRF) model [*Skamarock et al.*, 2005; *Skamarock and Klemp*, 2007] (Figure 8, solid line). A simulation with one domain covers March to October 2006 (to check the ability of the simulation to get the full monsoon life cycle, only one period centered about t_0 is here analyzed in detail) with a horizontal mesh size of 40 km and a domain centered at 14°N and 4.5°W, covering an area of 3800 km × 4800 km. The geographical data are from 5-min resolution USGS (United States Geophysical Survey) data. In the vertical, 35 unevenly spaced η levels are used and a complete set of physics parameterizations is used (*Kain and Fritsch* [1990, 1993] for the cumulus parametrization; *Chen and Dudhia* [2001] for the Noah land surface model; *Janjic* [2002; also The surface layer in the NCEP Eta model, paper presented at Eleventh Conference on Numerical Weather Prediction, American Meteorological Society, Boston, Massachusetts, 1996] for the Eta surface layer scheme; *Janjic* [1990, 2002, presented paper, 1996] for the Mellor Yamada Janjic PBL scheme; and *Mlawer et al.* [1997] and *Dudhia* [1989] for the longwave and shortwave radiation schemes, respectively). The initial and boundary conditions are taken from the NCEP Global Final (FNL) analyses, available every 6 hours on a 1° × 1° latitude longitude grid. Figure 8 shows that the observed fluctuations are well captured by the WRF model at the three stations (solid line), indicating that the model is able to reproduce the full monsoon cycle and its spatial variability. Indeed, at Niamey, the bias between the measurements and the simulation is -2.7 kg m^{-2}, the root mean square error (RMSE) is 3.1 kg m^{-2}, the cross correlation is 0.98. At Gao, the bias is -0.7 kg m^{-2}, the RMSE is 3.9 kg m^{-2}, the cross correlation is 0.95. At Tombouctou, the bias is -0.4 kg m^{-2}, the RMSE is 3.8 kg m^{-2}, the cross correlation is 0.94.

3.1.2. Evolution of the Intertropical Discontinuity

[25] In order to complement the analysis of the NCEP-2 reanalysis and to have a more accurate analysis of the westward propagation of the ITD southward retreat during June-July 2006, we use the WRF simulation covering June and July 2006. The equivalent potential temperature is used as a suited variable to diagnosing the ITD location since it allows to differentiating warm dry air masses of the harmattan from moist cooler air masses of the monsoon [*Dhonneur*, 1985]. For studying the propagation of the ITD perturbation, a two-dimensional (space and time) cross-correlation function has been applied to the time (t) versus latitude (y) equivalent potential temperature averaged between 4°E and 6°E (reference field θ_e^{ref}) and the time versus latitude equivalent potential temperature θ_e averaged over the same range of longitude (2°) but shifted westward by 2.5° until 15°W. The cross-correlation γ between θ_e^{ref} and θ_e writes

$$\gamma(\delta y, \delta t) = \int\int \theta_e^{ref}(y,t)\theta_e(y+\delta y, t+\delta t)dydt. \qquad (1)$$

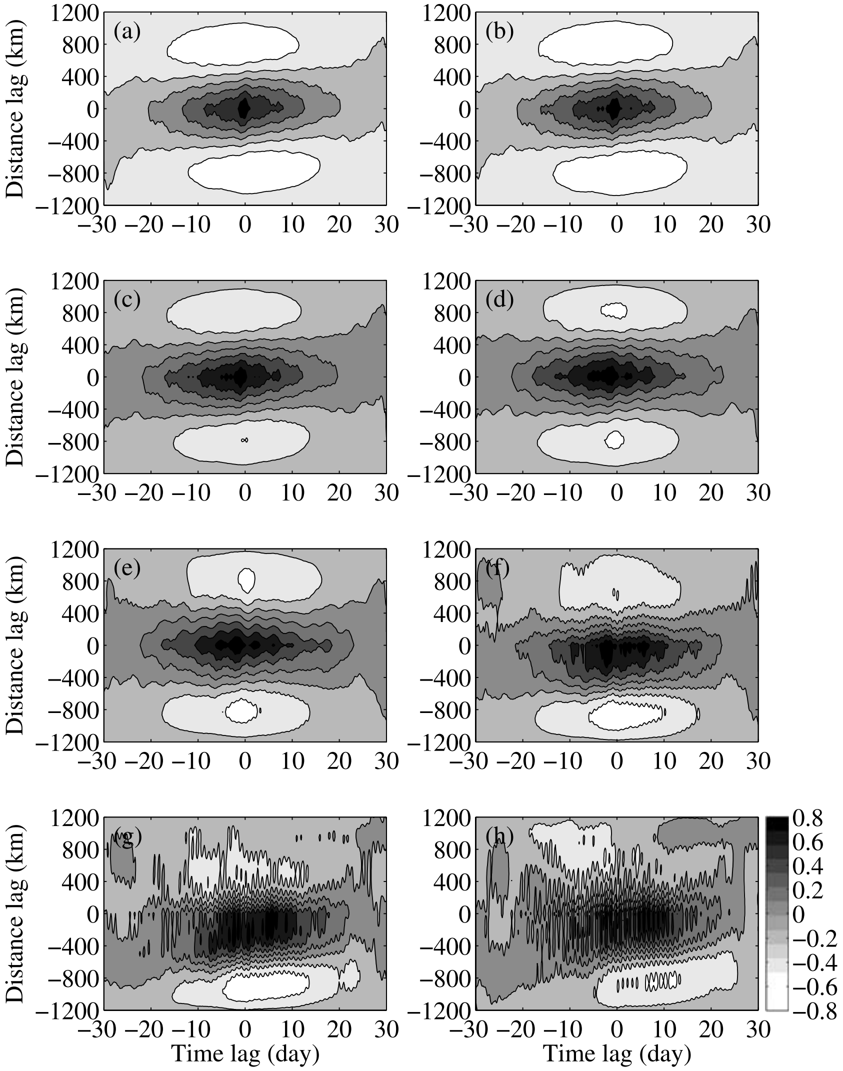

Figure 9. Cross-correlation function between the time versus latitude equivalent potential temperature simulated with WRF and averaged between 4°E and 6°E (reference field centered about 5°E) and the time versus latitude equivalent potential temperature averaged over the same range of longitude (2°) but shifted westward by 2.5° until 15°W, i.e., centered about (a) 2.5°E, (b) 0°E, (c) 2.5°W, (d) 5°W, (e) 7.5°W, (f) 10°W, (g) 12.5°W, and (h) 15°W.

The variables δy and δt are the latitudinal distance lag and time lag, respectively. Figure 9 shows the cross-correlation γ (δy, δt) and displays a marked maximum of positive cross-correlation γ until 10°W which marks the maximum range of propagation of the ITD perturbation signal.

[26] There is no longer correlation between the averaged equivalent potential temperature field centered about 5°E and the averaged equivalent potential temperature field west of 10°W. East of 10°W, the maximum correlation is always found at distance lag $\delta y = 0$ meaning that the ITD perturbation signal does not propagate latitudinally. Conversely, the time lag δt increases with increasing westward distance from 5°E longitude. Figure 10 shows the time lag δt corresponding to the cross-correlation maximum as a function of the distance from 5°E longitude.

[27] We see a linear trend until about 1600 km west of 5°E longitude. Farther to the west, the cross-correlation function becomes very noisy and thus the detection of the

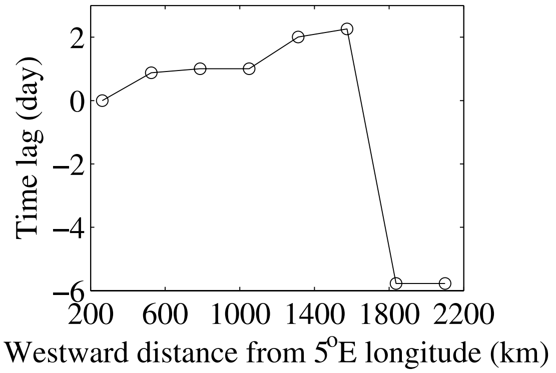

Figure 10. Time lag corresponding to the cross-correlation maximum of the equivalent potential temperature simulated with WRF as a function of the westward distance from 5°E longitude.

maximum correlation becomes meaningless as shown with the sharp jump in Figure 10. The slope of the linear fit until 1600 km west of 5°E longitude gives a propagation speed of the ITD perturbation signal equal to 6.8 m s^{-1}, which is consistent with the 5 m s^{-1} obtained with NCEP-2 reanalyses at 2.5° resolution.

3.2. African Easterly Jet and Orography Interaction

3.2.1. Data Analysis for 30 June 2006

[28] On 30 June 2006 the monsoon flow was documented before its northward propagation (3 days before the monsoon onset, $t_0 - 3$ days) over western Sahel and North Africa along a north-south transect by the French-German airborne Doppler lidar WIND on board of the DLR Falcon 20, flying at an altitude of 11 km with an aircraft ground speed of about 170 m s^{-1} [*Werner et al.*, 2001] (see Figure 1). The WIND instrument is operated at 10.6 μm, so the lidar signals are sensitive to micronic aerosols which are excellent tracers of the wind, therefore making WIND a relevant tool for the study of tropospheric dynamics [e.g., *Reitebuch et al.*, 2003; *Bastin et al.*, 2005b, 2006b; *Drobinski et al.*, 2006]. The Doppler lidar WIND provides wind radial velocity measurements along the line-of-sight (LOS) of the transmitted laser beam. The wind profile is obtained by conically scanning the LOS around the vertical axis with a fixed angle of 30° from nadir. The profile of the three-dimensional wind vector is calculated from the profiles of the LOS wind speeds using a velocity-azimuthal display (VAD) technique [*Reitebuch et al.*, 2001]. A full scan revolution of the line-of-sight takes 20 s, leading to a horizontal resolution of about 3.4 km between vertical profiles of the wind vector. The vertical resolution of the wind profiles is 250 m and the accuracy of the horizontal wind velocity is around 1 m s^{-1} [*Reitebuch et al.*, 2001]. The monsoon flow was also documented by means of operational radiosoundings performed by the national weather services (see Table 1; in this section, we only show thermodynamical vertical profiles from radiosoundings launched from Agadez (Niger), Cotonou (Benin), N'Djaména (Chad), Niamey (Niger), Ouagadougou (Burkina Faso) and Tamanrasset (Algeria), i.e., in the vicinity of the DLR Falcon 20 flight track; see Figure 1) and by a second WRF simulation starting 29 June 2006 at 1200 UTC and ending 1 July 2006 at 0000 UTC, similar to that described in section 3.1.1. One model domain, centered at 20°N and 0°E and covering an area of 4400 km × 4400 km, is used with a horizontal mesh size of 20 km.

[29] Figures 11 and 12 display a vertical cross section of the measured and simulated horizontal wind field (speed and direction) and of the lidar reflectivity and the simulated humidity and vertical wind along the leg flown by the Falcon aircraft on 30 June 2006 between 0850 and 1235 UTC (Figure 1).

[30] North of 30°N, the lidar reflectivity drops intermittently below values allowing a reliable retrieval of wind data (see blues "stripes" of reflectivity in Figure 12). These regions of low reflectivity are associated with the presence of clouds that prevent the lidar signal to go through. Looking at the simulated vertical velocity field (Figure 12b, colors), the regions of low reflectivity and cloud occurrence are associated with strong simulated convective updrafts. The very accurate colocation of the observed cloud-induced low reflectivity and the simulated intense updrafts contributes to give confidence in the WRF simulation.

[31] The flight track intersects the AEJ between Niamey (13.5°N) and about 26°N–27°N, which is also visible in Figure 13 with the change of wind direction between Agadez and Tamanrasset. The dry nature of the AEJ (Figure 2b) can be inferred from Figure 12a and by the radiosoundings (and their simulated counterpart) launched from Cotonou, Niamey, Agadez and Tamanrasset along a south-north axis and from Ouagadougou, Niamey and N'Djaména along a west-east axis since Figure 13 shows the relative humidity dropping below 5% above 5 km height, at Ouagadougou, Niamey, Agadez and Tamanrasset along the AEJ axis (Cotonou is used here to show a subtropical vertical profile outside the AEJ).

[32] The dry AEJ blows from the northeast at about 25 m s^{-1}, above the moist monsoon flow which blows from the south south of 18°N below about 1.8 km at about 6–8 m s^{-1}. The WRF simulation reproduces accurately the AEJ spatial extension, its direction but underestimates by about 5 m s^{-1} its intensity. At 18°N, the monsoon flow collides with the northeasterly harmattan which blows at about 10 m s^{-1}. At the ITD, a typical front head forms because of the quasi-stationary front associated with a very sharp horizontal gradient (the wind speed varies by 5 m s^{-1} over a horizontal range of about 20–30 km). At the ITD, Figure 12 shows that aerosols are lifted up at the top of the monsoon flow (see higher reflectivity and updraft at 18°N with a vertical velocity of +0.4 m s^{-1}) and reinjected within the monsoon flow south of the front by the front wake (see downdraft south of 18°N with a vertical velocity of −0.2 m s^{-1}) (see also *Flamant et al.* [2007] for other AMMA cases). Between 27°N and 19°N, the harmattan flow strengthens as it blows along the windward and leeward slopes of the Hoggar and Air massifs (11 m s^{-1}). This is visible on the measured or simulated horizontal wind speed (Figures 11 and 13 for Tamanrasset) but also on the vertical velocity field which displays a strong ascent on the wind ward side of the mountain range and a strong descent on the leeward side (Figure 12). The windward acceleration of the harmattan flow coincides with the presence of the AEJ blowing over and nearly perpendicular to the mountain range.

[33] One must note that during the flight, the atmospheric field does not evolve significantly north of the mountains so Figures 11 and 12 can be seen as a snapshot of the 1200 UTC atmospheric circulation.

3.2.2. Reduced Gravity Shallow Water Theory

[34] Figure 4d shows that, compared to the climatology, the northeasterly wind downstream of the Hoggar and Air massifs is much stronger on 30 June 2006. The region of the enhanced descending harmattan flow in the lee of the mountains, extends between about 2°E and 8°E and 19°N and 24°N, and includes the frontal zone between the northeasterly harmattan flow and the southwesterly monsoon flow. The intensification of the harmattan can be attributed to the unusual location of the AEJ which blows between 4 and 6 km height perpendicular to the mountain range (Hoggar and Air massifs) on 30 June 2006 (Figure 2), whereas it generally blows zonally over the Guinean coast at this period of the year (Figure 3). Indeed, as the AEJ blows over the mountain range, it produces a mountain wave at higher levels which forces and intensifies the

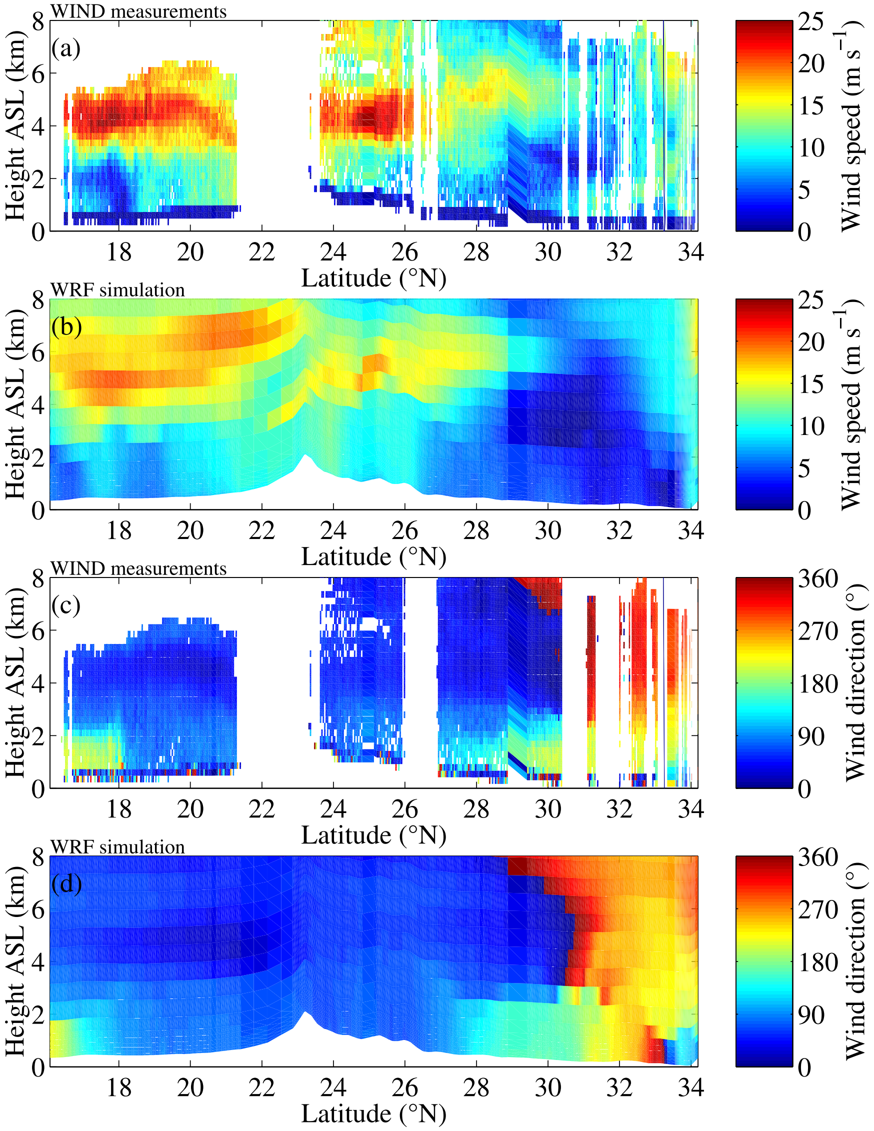

Figure 11. Vertical cross section of (a) wind speed and (c) wind direction retrieved from the WIND measurements along the leg flown by the DLR Falcon 20 between 0850 and 1235 UTC (Figure 1) after quality-control and debiasing procedure [*Dabas et al.*, 1998, 1999]. (b and d) Similar to Figures 11a and 11c but corresponding to the simulated data from WRF with 20-km mesh grid resolution.

harmattan flow near the ground that moves the monsoon flow downstream. This phenomenon can also be described in the framework of the reduced gravity shallow water (RGSW) theory [e.g., *Drobinski et al.*, 2001a] which assumes the flow to be in hydrostatic balance and bounded by a free surface. Then, if there are no variations in the coordinate direction parallel to the ridge axis, the steady state behavior of the system is governed by the shallow-water momentum and continuity equations,

$$U\frac{\partial U}{\partial y}+g'\frac{\partial h}{\partial y}+g'\frac{\partial e}{\partial y}=0 \tag{2}$$

$$\frac{\partial hU}{\partial y}=0. \tag{3}$$

Here y is the coordinate direction oriented perpendicular to the ridgeline (latitude, i.e., approximately the space coordinate along the flight track), U is the wind velocity in the y direction, g' the reduced gravity, h is the thickness of the flow, i.e., the atmospheric boundary layer (ABL) depth (well defined by the 318 K isentropes; see Figure 12b) and e is the mountain height. By combining equations (2) and (3), we obtain the following equation [*Durran*, 1990]:

$$\left(1-\frac{1}{(Fr)^2}\right)\frac{\partial(e+h)}{\partial y}=\frac{\partial e}{\partial y}, \tag{4}$$

where Fr is the Froude number defined as $Fr = U/(g'h)^{1/2}$, i.e., the ratio of the flow velocity to the speed of propagation of linear shallow-water gravity waves. According to equation (4), the ABL top can either rise or fall as the

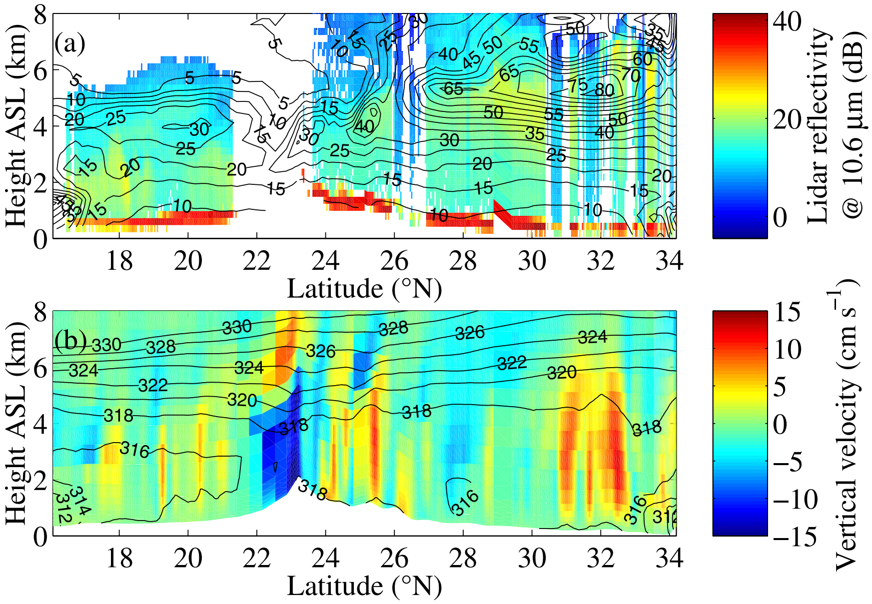

Figure 12. Vertical cross section of (a) lidar reflectivity retrieved from the WIND measurements along the leg flown by the DLR Falcon 20 between 0850 and 1235 UTC (Figure 1) and relative humidity simulated with WRF with 20-km mesh grid resolution at 1000 UTC (isocontours) and (b) simulated vertical velocity at 1000 UTC along the leg flown by the DLR Falcon 20 (color shading) and simulated isentropes (isocontours).

harmattan encounters rising bottom topography, depending on the magnitude of Fr. Indeed, the steady state momentum equation (see equation (2)) requires a three-way balance between nonlinear advection (first term), pressure gradient forces arising from changes in the flow depth (second term) and the component of gravity parallel to the sloping topography (third term). From equation (2), one can easily show that $-Fr^2$ is the ratio of the magnitude of nonlinear advection to the pressure gradient generated by changes in the fluid depth. For $Fr > 1$ ($Fr < 1$) nonlinear advection dominates the pressure gradient term and the three-way balance is satisfied when the flow is accelerated in the same (opposite) direction as the gravitational force. The main assumption of the RGSW theory is the absence of exchanges between these the ABL and free troposphere, which depends on the strength of the potential temperature inversion at the ABL top. In our case the potential temperature inversion at the ABL top is about 5 K km^{-1} (see Figure 13), which has proved to be large enough to prevent significant exchanges between the ABL and the free troposphere (see *Drobinski et al.* [2001b] and *Corsmeier et al.* [2005] for further discussion). The flow is called subcritical (supercritical) when the local Froude number is lower (greater) than unity. When the flow transitions from a supercritical to a subcritical regime, a hydraulic jump occurs, characterized by a sharp wind speed deceleration and layer depth deepening [e.g., *Drobinski et al.*, 2001a]. Note that other authors have used the concept of diving streamline or diving isentrope to represent a critical level separating a stratified flow below and a less stratified flow above in downslope wind analyses [*Smith*, 1985]. Whenever $\mathrm{Fr} > 1$ (supercritical conditions), $\partial e/\partial y > 0$ implies that $\partial\,(h + e)/\partial y > 0$, so that $h + e$ and e are correlated (i.e., exhibit similar trends, increase or decrease at the same time). Whenever $Fr < 1$ (subcritical conditions), $\partial e/\partial y > 0$ implies that $\partial\,(h + e)/\partial y < 0$, so that $h + e$ and e are anticorrelated. Figure 14 displays the Froude number calculated using the 318-K-isentrope height and the wind simulated with WRF. Since a nonnegligible wind shear is to be expected between the surface and 318-K-isentrope height, we use an average wind speed below the 318-K isentrope given by *Drobinski et al.* [2001b],

$$\overline{U} = \frac{1}{h}\int_{e}^{e+h} U(z)dz, \qquad (5)$$

where $U(z)$ is the wind speed in the ABL. Figure 14 shows that the flow is supercritical just after the mountain (between 22.3°N and 23.4°N) where Fr is significantly larger than unity. In the other parts of the domain, the flow is subcritical because the values of Fr are much smaller unity.

[35] In fact, three regions can be identified.

[36] 1. Upstream of the mountain ridge, north of 23.4°N, trends in e and $h + e$ are anticorrelated, suggesting that the flow is subcritical. It is also confirmed by the harmattan acceleration as it ascends the northern slope of the mountains.

[37] 2. From 23.4°N to 22.3°N, the trends in e and $h + e$ are observed to be correlated, suggesting that the flow is supercritical. It is also confirmed by the harmattan acceleration as it descends the northern slope of the mountains (11 m s^{-1}).

[38] 3. South of 22.3°N, down to the ITD, trends in e and $h + e$ are anticorrelated, suggesting that the flow is subcritical. The transition from supercritical to subcritical conditions forms a hydraulic jump, associated with flow

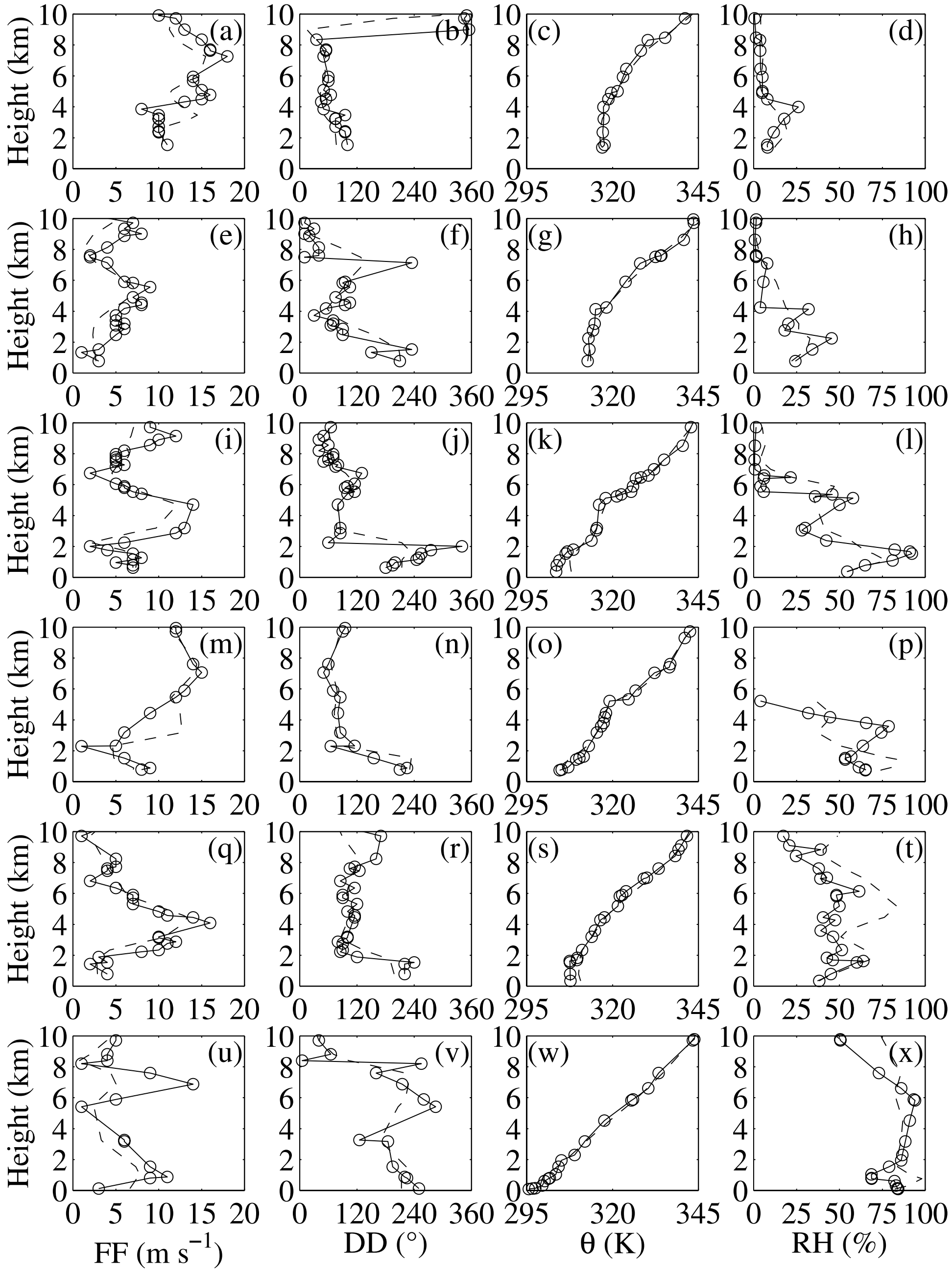

Figure 13. Vertical profiles of (a, e, i, m, q, and u) wind speed (FF) and (b, f, j, n, r, and v) direction (DD), (c, g, k, o, s, and w) potential temperature (θ) and (d, h, l, p, t, and x) relative humidity (RH) from the radiosoundings launched on 30 June 2006 at 1200 UTC from Tamanrasset (Figures 13a–13d), Agadez (Figures 13e–13h), Niamey (Figures 13i–13l), Ouagadougou (Figures 13m–13p), N'Djaména (Figures 13q–13t), and Cotonou (Figures 13u–13x) (see Figure 1). The solid line with the circles corresponds to the radiosounding data, and the dashed line corresponds to the WRF simulation with 20-km mesh grid resolution.

deceleration (Figure 11), enhanced turbulence (identified with large vertical velocity; see Figure 12).

[39] The 318-K-isentrope height, wind speed and terrain elevation evolution downstream of the Hoggar and Air massifs are consistent with that expected in the RGSW theory framework. The slope-induced acceleration of the harmattan downstream of the mountains may thus contribute to move southward the monsoon flow and delay its northward propagation.

[40] In order to assess nonambiguously the role of the interactions between the AEJ and the mountains on the harmattan acceleration, we compared the 2006 unusual onset period to the more classical 2005 onset period, similar to the climatology with a more zonal and southward AEJ, 5 m s^{-1} weaker than in 2006 and an onset date t_0 = 22 June

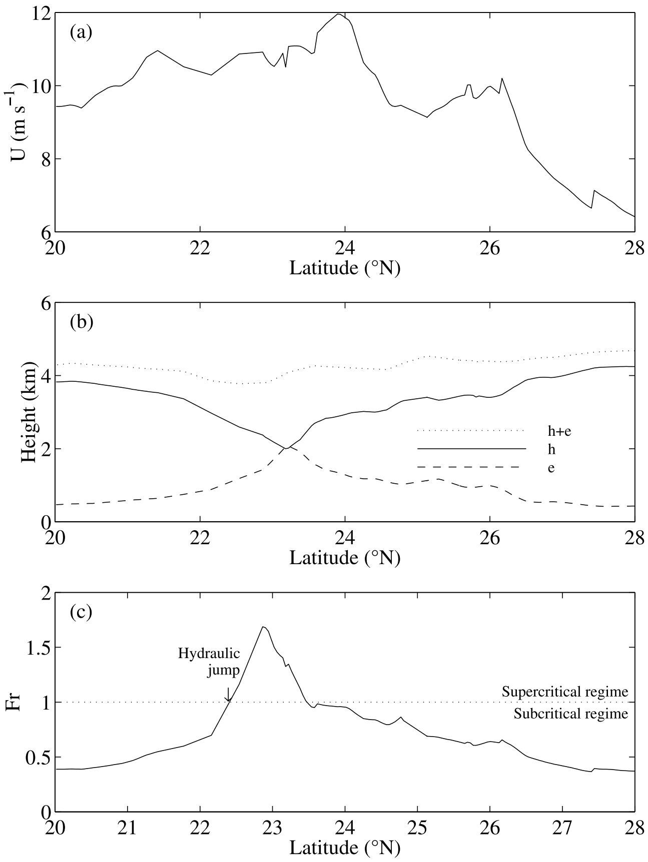

Figure 14. Average wind speed $\overline{U}$ on 30 June 2006 at 1200 UTC computed from equation (5): (a) elevation of the topography (*e*, dashed line), (b) height of the 318-K isentrope (*h*, solid line) and *e* + *h* (dotted line), and (c) Froude number with the dashed line indicating the critical value of 1. The data are from the WRF simulation.

2005 (the climatological date being 24 June) (NCEP reanalysis and WRF simulation not shown). We computed the normalized harmattan (HAR) intensity HAR/WAM averaged over the boxes (5°E–10°E;22°N–25°N) (harmattan) and (2°E–5°E;12°N–15°N) (WAM) and the lower levels. This ratio gives the relative intensity of the harmattan to the WAM. The ratio HAR/WAM = 0.77 in 2005 and 1.30 in 2006. This shows the impact of the AEJ/orography interaction on the intensity of the harmattan and thus its capacity to maintain the monsoon flow to the south of its climatological position.

[41] Finally, one must note at this point that the role of the orography on the WAM onset identified by *Sultan and Janicot* [2003] and *Drobinski et al.* [2005] is the dynamical deepening of the Saharan heat low by the lee cyclone induced by the Hoggar massif which contributes to the northward propagation of the monsoon. In the present article, the orography has a different impact on the monsoon in the Niger/Mali region, since the interaction between the mountains on the AEJ reinforces the harmattan flow by the generation of mountain waves in the lee of the Hoggar/Air massifs. The stronger harmattan flow acts as a front moving backward the monsoon flow causing the delay of its northward propagation. So the process described in the present article and that detailed by *Sultan and Janicot* [2003] and *Drobinski et al.* [2005] are basically different but may coexist.

4. Conclusion

[42] This paper investigates the role of scale interactions and orography on the late northward migration of the West African monsoon in June–July 2006, in the region of Niger and Mali. Compared to a 28-year climatology of the 10-m and 500-hPa wind fields, the end of June and beginning of July 2006 displays unusual characteristics: (1) the Libyan anticyclone is shifted westward compared to the climatology and the associated African Easterly Jet (AEJ) blows from the northeast along a narrow northeast/southwest oriented band whereas it generally blows zonally at about 8°N; (2) the intertropical discontinuity (ITD), defined as the interface between the cool moist southwesterly monsoon flow and the warm and dry northeasterly harmattan flow, is located until mid-July around 17°N, which is approximately its climatological location in May-June instead of 20°N in July; and (3) the surface wind downstream of the main mountain ridge of the Hoggar and Air massifs is stronger by about 4 m s^{-1} than the climatology during about 1 week after the climatological date of the WAM onset date.

[43] The multiscale dynamics analysis of the interactions between the synoptic environment and the structure of the monsoon flow is conducted using the observations (radiosoundings, Doppler lidar data) collected on 30 June 2006 in the framework of the African Monsoon Multidisciplinary Analysis (AMMA) program, as well as of numerical simulations using the Weather Research and Forecast (WRF) mesoscale model. The data and simulations show a deep atmospheric boundary layer (ABL) (4 km deep), north (i.e., upstream) of the Hoggar and Air massifs, whereas the shallow harmattan flow has the characteristics of a downslope wind blowing at about 11 m s^{-1} embedded in a shallow ABL (2 km deep) on the leeward slope of the mountain range. South of 22.3°N, the ABL deepens again (4 km deep), associated with flow deceleration (9 m s^{-1}). The observations and simulations provide a large body of evidence that downslope harmattan flow created thinning/thickening ABL and accelerations/decelerations reminiscent of mountain wave/hydraulic theory.

[44] The persistence of the reinforcement of the harmattan flow downstream of the Hoggar and Air mountains, due to the interaction between the AEJ and the orography, is assessed using NCEP analyses in June and July 2006 and contributes to the ITD southward retreat with respect to the climatology. This phenomenon starts on 25 June and ends on 3 July 2006 which marks the beginning of the onset of the WAM and its northward propagation. The analyses also reveal a westward propagation of the southward ITD retreat at about 5 m s^{-1}, coincident with the passage of an AEW over the target area. We thus suggest that the ITD southward migration is due to (1) the interaction between the AEJ and the orography, which causes the reinforcement of the harmattan, and (2) an interaction between the ITD and African Easterly waves which contributes to propagate westward the ITD southward retreat. Finally, the combined effect of the enhanced harmattan which prevents the northward propagation of the ITD and the dry air intrusion which

inhibits organized convection may explain part of the late WAM onset in summer 2006 in the Niger/Mali region.

[45] **Acknowledgments.** We are thankful to the three anonymous referees and B. Ballish (NCEP), who helped to improve the manuscript significantly, as well as to N. Ascencio (CNRM) for fruitful discussions. We would also like to thank B. Romand (LMD/IPSL), M.L. Denneulin (CNRM), and E. Nagel (DLR) for assistance in operation of the WIND system, the pilots of the DLR flight facility R. Welser and M. Grossrubatscher, the Falcon technician, and the great support of A. Giez (DLR). On the basis of French initiative, AMMA was built by an international scientific group and is currently funded by a large number of agencies, especially from France, U.K., Germany, United States, and Africa. It has been the beneficiary of a major financial contribution from the European Community's Sixth Framework Research Program. Detailed information on scientific coordination and funding is available on the AMMA International website http://www.amma-international.org.

References

Bastin, S., P. Drobinski, A. M. Dabas, P. Delville, O. Reitebuch, and C. Werner (2005a), Impact of the Rhône and Durance valleys on sea-breeze circulation in the Marseille area, *Atmos. Res.*, *74*, 303–328.

Bastin, S., C. Champollion, O. Bock, P. Drobinski, and F. Masson (2005b), On the use of GPS tomography to investigate water vapor variability during a Mistral/sea breeze event in southeastern France, *Geophys. Res. Lett.*, *32*, L05808, doi:10.1029/2004GL021907.

Bastin, S., C. Champollion, O. Bock, P. Drobinski, and F. Masson (2006a), Diurnal cycle of water vapor as documented by a dense GPS network in a coastal area during ESCOMPTE-IOP2, *J. Appl. Meteorol. Climatol.*, *46*, 167–182.

Bastin, S., P. Drobinski, V. Guénard, J. L. Caccia, B. Campistron, A. M. Dabas, P. Delville, O. Reitebuch, and C. Werner (2006b), On the interaction between sea breeze and summer mistral at the exit of the Rhône valley, *Mon. Weather Rev.*, *134*, 1647–1668.

Bock, O., F. Guichard, S. Janicot, J. P. Lafore, M. N. Bouin, and B. Sultan (2007), Multiscale analysis of precipitable water vapor over Africa from GPS data and ECMWF analyses, *Geophys. Res. Lett.*, *34*, L09705, doi:10.1029/2006GL028039.

Chen, F., and J. Dudhia (2001), Coupling and advanced and-surface/hydrology model with the Penn State/NCAR MM5 modeling system. Part I: Model descriptiion and implementation, *Mon. Weather Rev.*, *129*, 569–585.

Corsmeier, U., R. Behrendt, P. Drobinski, and C. Kottmeier (2005), The mistral and its effect on air pollution transport and vertical mixing, *Atmos. Res.*, *74*, 275–302.

Dabas, A., P. Drobinski, and P. H. Flamant (1998), Chirp-induced bias in velocity measurements by a coherent Doppler CO_2 lidar, *J. Atmos. Oceanic Technol.*, *15*, 407–415.

Dabas, A., P. Drobinski, and P. H. Flamant (1999), Adaptive filters for frequency estimate of heterodyne Doppler lidar returns: Recursive implementation and quality control, *J. Atmos. Oceanic Technol.*, *16*, 361–372.

Dhonneur, G. (1985), Treatise on tropical meteorology: Application to the special case of the West and Central Africa, report, 152 pp., Météo-France, Paris.

Diedhiou, A., S. Janicot, A. Viltard, P. de Felice, and H. Laurent (1999), Easterly wave regimes and associated convection over West Africa and tropical Atlantic: Results from the NCEP/NCAR and ECMWF reanalysis, *Clim. Dyn.*, *15*, 795–822.

Drobinski, P., J. Dusek, and C. Flamant (2001a), Diagnostics of hydraulic jump and gap flow in stratified flows over topography, *Boundary Layer Meteorol.*, *98*, 475–495.

Drobinski, P., C. Flamant, J. Dusek, P. H. Flamant, and J. Pelon (2001b), Observational evidence and modeling of an internal hydraulic jump at the atmospheric boundary layer top during a Tramontane event, *Boundary Layer Meteorol.*, *98*, 497–515.

Drobinski, P., B. Sultan, and S. Janicot (2005), Role of the Hoggar massif on the West African monsoon onset, *Geophys. Res. Lett.*, *32*, L01705, doi:10.1029/2004GL020710.

Drobinski, P., S. Bastin, A. M. Dabas, P. Delville, and O. Reitebuch (2006), Variability of the three-dimensional sea-breeze structure in southeastern France: Observations and evaluation of empirical scaling laws, *Ann. Geophys.*, *24*, 1783–1799.

Dudhia, J. (1989), Numerical study of convection observed during the winter monsoon experiment using a mesoscale two-dimensional model, *J. Atmos. Sci.*, *46*, 3077–3107.

Durran, D. R. (1990), Mountain waves and downslope winds, in *Atmospheric Processes Over Complex Terrain*, *Meteorol. Monogr.*, vol. 23, pp. 59–81, Am. Meteorol. Soc., Boston, Mass.

Flamant, C., J. P. Chaboureau, D. J. Parker, C. M. Taylor, J. P. Cammas, O. Bock, F. Timouk, and J. Pelon (2007), Airborne observations of the impact of a convective system on the planetary boundary layer thermodynamics and aerosol distribution in the inter-tropical discontinuity region of the West African monsoon, *Q. J. R. Meteorol. Soc.*, *133*, 1175–1189.

Hagos, S. M., and K. H. Cook (2007), Dynamics of the West African monsoon jump, *J. Clim.*, *20*, 5264–5284.

Hastenrath, S. (1995), *Climate Dynamics of the Tropics*, 488 pp., Kluwer Acad., Norwell, Mass.

Hsieh, J., and K. H. Cook (2005), Generation of African Easterly Wave disturbances: Relationship to the African Easterly Jet, *Mon. Weather Rev.*, *133*, 1311–1327.

Janicot, S., S. Trzaska, and I. Poccard (2001), Summer Sahel-ENSO teleconnection and decadal time scale SST variations, *Clim. Dyn.*, *18*, 303–320.

Janicot, S., et al. (2008), Large-scale overview of the summer monsoon over West Africa during the AMMA field experiment in 2006, *Ann. Geophys.*, *26*, 2569–2595.

Janjic, Z. I. (1990), The step-moutain coordinate: Physical package, *Mon. Weather Rev.*, *118*, 1429–1443.

Janjic, Z. I. (2002), Nonsingular Implementation of the Mellor-Yamada Level 2.5 Scheme in the NCEP Meso model, *Off. Note 437*, 61 pp., Natl. Cent. For Environ. Predict., Camp Springs, Md.

Kain, J. S., and J. M. Fritsch (1990), A one-dimensional entraining/detraining plume model and application in convective parameterization, *J. Atmos. Sci.*, *47*, 2784–2802.

Kain, J. S., and J. M. Fritsch (1993), Convective parameterization for mesoscale models: The 17 Kain-Fritsch scheme, in *The Representation of Cumulus Convection in Numerical Models*, *Meteorol. Monogr.*, vol. 24, pp. 165–170, Am. Meteorol. Soc., Boston, Mass.

Kalnay, E., et al. (1996), The NCEP/NCAR 40-Year Reanalysis Project, *Bull. Am. Meteorol. Soc.*, *77*, 437–471.

Kanamitsu, M., W. Ebisuzaki, J. Woollen, S. K. Yang, J. J. Hnilo, M. Fiorino, and G. L. Potter (2002), NCEP-DEO AMIP-II Reanalysis (R-2), *Bull. Am. Meteorol. Soc.*, *83*, 1631–1643.

Lebel, T., F. Delclaux, L. Le Barb, and J. Polcher (2000), From GCM scales to hydrological scales: Rainfall variability in West Africa, *Stochastic Environ. Res. Risk Assess.*, *14*, 275–295.

Mlawer, E. J., S. J. Taubman, P. D. Brown, M. J. Iacono, and S. A. Clough (1997), Radiative transfer for inhomogeneous atmosphere: RRTM, a validated correlated-k model for the longwave, *J. Geophys. Res.*, *102*(D14), 16,663–16,682.

Mohr, K. I. (2004), Interannual, monthly, and regional variability in the wet season diurnal cycle of precipitation in sub-Saharan Africa, *J. Clim.*, *17*, 2441–2543.

Parker, D. J., R. R. Burton, A. Diongue-Niang, R. J. Ellis, M. Felton, C. M. Taylor, C. D. Thorncroft, P. Bessemoulin, and A. M. Tompkins (2005), The diurnal cycle of the West African monsoon circulation, *Q. J. R. Meteorol. Soc.*, *131*, 2839–2860.

Peyrillé, P., and J. P. Lafore (2007), An idealized two-dimensional framework to study the West African monsoon. Part II: Large-scale advection and the diurnal cycle, *J. Atmos. Sci.*, *64*, 2783–2803.

Peyrillé, P., J. P. Lafore, and J. L. Redelsperger (2007), An idealized two-dimensional framework to study the West African monsoon. Part I: Validation and key controlling factors, *J. Atmos. Sci.*, *64*, 2765–2782.

Rácz, Z., and R. K. Smith (1999), The dynamics of heat lows, *Q. J. R. Meteorol. Soc.*, *125*, 225–252.

Ramel, R., H. Gallée, and C. Messager (2006), On the northward shift of the West African monsoon, *Clim. Dyn.*, *26*, 429–440.

Reed, R. J., D. C. Norquist, and E. E. Recker (1977), The structure and properties of African wave disturbances as observed during phase III of GATE, *Mon. Weather Rev.*, *105*, 17–33.

Reitebuch, O., C. Werner, I. Leike, P. Delville, P. H. Flamant, A. Cress, and D. Engelbart (2001), Experimental validation of wind profiling performed by the airborne 10.6 m-heterodyne Doppler lidar WIND, *J. Atmos. Oceanic Technol.*, *18*, 1331–1344.

Reitebuch, O., H. Volkert, C. Werner, A. M. Dabas, P. Delville, P. Drobinski, P. H. Flamant, and E. Richard (2003), Determination of airflow across the Alpine Ridge by a combination of Doppler lidar, routine radiosounding, and numerical simulation, *Q. J. Roy. Meteorol. Soc.*, *129*, 715–727.

Roca, R., J. P. Lafore, C. Piriou, and J. L. Redlesperger (2005), Extratropical dry-air intrusions into the West African monsoon midtroposphere: An important factor for the convective activity over the Sahel, *J. Atmos. Sci.*, *62*, 390–407.

Sijikumar, S., P. Roucou, and B. Fontaine (2006), Monsoon onset over Sudan-Sahel: Simulation by the regional scale model MM5, *Geophys. Res. Lett.*, *33*, L03814, doi:10.1029/2005GL024819.

Skamarock, W. C., and J. B. Klemp (2007), A time-split nonhydrostatic atmospheric model for research and NWP applications, *J. Comput. Phys.*, *227*, 3465–3485.

Skamarock, W. C., J. B. Klemp, J. Dudhia, D. O. Gill, D. M. Barker, W. Wang, and J. G. Powers (2005), A description of the Advanced Research WRF version 2, *NCAR Tech. Note NCAR/TN-468+STR*, 88 pp., Natl. Cent. for Atmos. Res., Boulder, Colo.

Smith, R. B. (1985), On severe downslope winds, *J. Atmos. Sci.*, *42*, 2597–2603.

Sultan, B., and S. Janicot (2003), The West African monsoon dynamics. Part II: The "preonset" and "onset" of the summer monsoon, *J. Clim.*, *16*, 3407–3427.

Sultan, B., S. Janicot, and P. Drobinski (2007), Characterization of the diurnal cycle of the West African monsoon around the monsoon onset, *J. Clim.*, *20*, 4014–4032.

Thorncroft, C. D., J. P. Lafore, G. Berry, R. Roca, F. Guichard, M. Tomasini, and N. Asencio (2007), Overview of African weather systems during the summer 2006, *CLIVAR Exchanges*, *12*, 18–20.

Werner, C., et al. (2001), WIND instrument, *Opt. Eng.*, *40*, 115–125.

Yang, G. Y., and J. Slingo (2001), The diurnal cycle in the tropics, *Mon. Weather Rev.*, *129*, 784–801.

Zehnder, X., D. M. Powell, and E. A. B. Eltahir (1999), The interaction of easterly waves, orography, and the intertropical convergence zone in the genesis of Eastern Pacific Tropical cyclones, *Mon. Weather Rev.*, *127*, 1566–1585.

Zheng, X., and E.A.B. Eltahir (1998), The role of vegetation in the dynamics of West African monsoons, *J. Clim.*, *11*, 2078–2096.

S. Bastin and O. Bock, Service d'Aéronomie, Institut Pierre Simon Laplace, UPMC, UVSQ, CNRS, F-91128 Palaiseau CEDEX, France.

A. Dabas, Centre National de Recherches Météorologiques, Météo-France, F-31057 Toulouse CEDEX 1, France.

P. Delville, Division Technique, Institut National des Sciences de l'Univers, CNRS, F-92195 Meudon, France.

P. Drobinski, Laboratoire de Météorologie Dynamique, Institut Pierre Simon Laplace, École Polytechnique, F-91128 Palaiseau CEDEX, France. (philippe.drobinski@lmd.polytechnique.fr)

S. Janicot and B. Sultan, Laboratoire d'Océanographie et du Climat: Expérimentation et Approches Numériques, Institut Pierre Simon Laplace, UPMC, IRD, MNHN, CNRS, F-75252 Paris, France.

O. Reitebuch, Institut für Physik der Atmosphäre, Deutsches Zentrum für Luft- und Raumfahrt, D-82234 Wessling, Germany.